



Mechanical instability induced by water weakening in laboratory fluid injection tests

C. David, J. Dautriat, J. Sarout, C. Delle Piane, Beatriz Menendez, R. Macault, D. Bertauld

► To cite this version:

C. David, J. Dautriat, J. Sarout, C. Delle Piane, Beatriz Menendez, et al.. Mechanical instability induced by water weakening in laboratory fluid injection tests. *Journal of Geophysical Research: Solid Earth*, 2015, 120 (6), pp.4171-4188. 10.1002/2015JB011894 . hal-03266059

HAL Id: hal-03266059

<https://hal.science/hal-03266059>

Submitted on 9 Feb 2023

HAL is a multi-disciplinary open access archive for the deposit and dissemination of scientific research documents, whether they are published or not. The documents may come from teaching and research institutions in France or abroad, or from public or private research centers.

L'archive ouverte pluridisciplinaire **HAL**, est destinée au dépôt et à la diffusion de documents scientifiques de niveau recherche, publiés ou non, émanant des établissements d'enseignement et de recherche français ou étrangers, des laboratoires publics ou privés.

Mechanical instability induced by water weakening in laboratory fluid injection tests

David, C. ^{a*}, Dautriat, J. ^b, Sarout, J. ^b, Delle Piane, C. ^b, Menéndez, B. ^a, Macault, R. ^{a,b},
Bertauld, D. ^{a,b}

^a Université de Cergy-Pontoise, Laboratoire Géosciences et Environnement Cergy, FRANCE

^b CSIRO Energy, Perth, AUSTRALIA

* Corresponding author: christian.david@u-cergy.fr

Abstract

To assess water-weakening effects in reservoir rocks, previous experimental studies have focused on changes in the failure envelopes derived from mechanical tests conducted on rocks fully saturated either with water or with inert fluids. So far little attention has been paid to the mechanical behavior during fluid injection under conditions similar to enhanced oil recovery operations. We studied the effect of fluid injection on the mechanical behavior of the weakly consolidated Sherwood sandstone in laboratory experiments. Our specimens were instrumented with 16 ultrasonic P-wave transducers for both passive and active acoustic monitoring during loading and fluid injection to record the acoustic signature of fluid migration in the pore space and the development of damage. Calibration triaxial tests were conducted on three samples saturated with air, water or oil. In a second series of experiments, water and inert oil were injected into samples critically-loaded up to 80% or 70% of the dry or oil-saturated compressive strength, respectively, to assess the impact of fluid migration on mechanical strength and elastic properties. The fluids were injected with a low back pressure to minimize effective stress variations during injection. Our observations show that creep

takes place with a much higher strain rate for water injection compared to oil injection. The most remarkable difference is that water injection in both dry and oil-saturated samples triggers mechanical instability (macroscopic failure) within half an hour whereas oil injection does not after several hours. The analysis of X-ray CT images of post-mortem samples revealed that the mechanical instability was probably linked to loss of cohesion in the water invaded region.

1. Introduction

It has long been recognized that the nature of the fluid present in the pore space of a reservoir rock can have a significant influence on its mechanical behavior. Water weakening is a well-known phenomenon that has been recognized in several geological settings, affecting different rock types, like sandstones and carbonates. For example Risnes et al. [2005] focused on the mechanical behavior of chalk to highlight the importance of water-weakening effects in the subsidence observed during the production and stimulation of the Ekofisk hydrocarbon reservoir in the southern part of the North Sea. They showed that the failure envelope for Ekofisk chalk samples depends on the nature of the saturating fluid, and that the chalk is significantly weaker when water is saturating the rock pore space than for any other saturating fluid. Different weakening mechanisms can operate when rocks exhibit water sensitivity, among them chemical and stress effects on mineral solubility (especially calcite) [Risnes et al., 2005], stress corrosion effects permitting easier crack propagation [Atkinson and Meredith, 1987; Zhu and Wong, 1997], adsorption effects at grain surfaces [Orowan, 1944; Rehbinder et al., 1948; Baud et al., 2000], water-clay mineral interactions and capillary effects [Schmitt et al., 1994]. To study water weakening in the laboratory, a classical method is to compare the mechanical behavior of rocks with different saturating fluids in standard triaxial tests under comparable effective confining pressure, and to infer the failure envelopes.

51 Doing so, Baud et al. [2000] found for several sandstones that water weakening affects both
52 the strength (i.e. low mechanical strength in water-saturated rocks) and the elastic moduli (i.e.
53 low elastic moduli in water-saturated rocks).

54 Little attention has been paid so far to fluid substitution processes in a reservoir at depth and
55 the resulting consequences in terms of mechanical stability. This issue is crucial for the
56 development of enhanced oil recovery strategies in partially depleted reservoirs. Indeed a
57 widespread method to maintain reservoir pressure during production is to inject water into the
58 reservoir [Donnez, 2012]. Nevertheless injecting water can have a strong impact on the
59 reservoir mechanical stability: a good example of problems that might occur is the increase of
60 subsidence rate observed for the Ekofisk reservoir when water was injected to recover its
61 original pore pressure [Doornhof et al., 2006]. Therefore an integrated study combining
62 mechanical characterization and fluid migration monitoring in porous rocks is desirable. The
63 idea is to isolate the water weakening effect during fluid injection from any other, especially
64 effective stress variations. In contrast to former experimental studies on water weakening
65 based on triaxial testing on fluid saturated rocks, our approach - partly inspired by Stanchits et
66 al. [2011] - consists in injecting water in reservoir rocks with minimum perturbation of the
67 stress, to analyze how weakening effects progressively affect their mechanical integrity under
68 conditions similar to fluid injection/withdrawal in real reservoirs. One key question is to
69 understand the damage that water weakening produces and if it can lead to localized
70 deformation structures like shear fractures or compaction bands. Another key question is
71 whether continuous acoustic monitoring is capable of recording the fluid substitution process
72 and the associated damage when water weakening is active in rocks. To answer these
73 questions, we developed an original experimental protocol designed to highlight the
74 weakening effects of fluid injection.

2. Petrophysical and mechanical properties of the selected rock

We selected for our study the weakly-consolidated Sherwood sandstone, also named Otter Sherwood sandstone, a fairly good analog for an actual reservoir rock. The Sherwood sandstone formation is produced at a depth of approximately 1500 m in the Wytch Farm Oil Field, the only onshore oil field operated in the UK. The Sherwood sandstone outcrops in South-West of England and was sampled directly at the Ladram Bay cliffs. Quartz and Felspar are the major minerals in the rock composition, with also a significant amount of detrital clays (**Table 1**, see also Nguyen et al., 2014). The Sherwood sandstone has a mean porosity of 30%, an average grain diameter of 120 μm and an anisotropic permeability, with 200 mD and 350 mD normal and parallel to the bedding, respectively. The Sherwood sandstone is poorly consolidated and needs to be handled with care during coring and preparation for laboratory experiments.

The hydro-mechanical behavior of the Sherwood sandstone was investigated thoroughly by Nguyen et al. [2014] in triaxial experiments with controlled stress paths. The failure envelope [Wong et al., 1997] for water-saturated samples was obtained under drained conditions and the onset of grain-crushing and pore collapse occurs at a critical pressure of $P^*=40$ MPa as determined by Nguyen et al. [2014]. In addition to its low mechanical strength, we also selected this rock because of its sensitivity to water: for example the critical pressure P^* is much higher for the dry Sherwood sandstone (> 60 MPa) than for the water saturated rock.

The P wave velocity anisotropy was investigated at room conditions through measurements for ray paths with different angle with respect to the bedding. The dry Sherwood sandstone exhibits a significant velocity anisotropy (about 15%) with a minimum velocity for P-waves travelling perpendicular to the bedding (1250 m/s) and a maximum velocity for travel paths parallel to bedding (1470 m/s). This anisotropy vanishes when the rock sample is saturated with water, and velocity for all travel paths shows a fairly similar value (~ 2000 m/s). This

contrast in anisotropy can be explained by pore shape anisotropy as shown by Louis et al. [2003]: when saturated with water the pores with anisotropic shape become stiffer and have a smaller effect on the overall elastic anisotropy. We have also measured the evolution of P-wave velocity for partially saturated samples and found that in the low water saturation range ($S_w < 55\%$) the P-wave velocity is lower than that of the dry rock, then increases to a higher value close to full saturation. P-wave velocity anisotropy and variation with saturation need to be taken into account for the understanding and modeling of the injection experiments reported below.

3. Experimental approach

3.1. Experimental set-up

Series of mechanical tests were conducted at the CSIRO's rock mechanics laboratory (Perth, Australia) using a Sanchez Technologies triaxial rig [Sarout et al., 2010; Sarout et al., 2014] on rock specimens with 38 mm nominal diameter and 80 mm nominal length. All samples were cored in a direction perpendicular to the bedding. During each mechanical test, the mean axial strain is measured and averaged over the sample length through three external displacement sensors, and the local radial strain by an internal cantilever sensor attached at mid-height to the sample. The average volumetric strain is computed from axial and radial strains. All of the mechanical parameters are controlled and monitored in real time on a computer with a LabVIEW interface. A special jacket design is used to isolate the sample from the confining fluid, with provision for attaching 16 piezoelectric sensors directly to the sample's surface and distributed on four different planes. In our experiments only P-wave transducers, with a diameter of 9 mm and a mean resonant frequency of 0.5 MHz, were used. They are connected to an Applied Seismology Consultants ultrasonic monitoring system which can work in two different modes: in the passive mode the system records all micro-

seismic events (above a pre-defined energy threshold) which occur in the sample during loading; in the active (or survey) mode the system works in a transmitter-receiver configuration, with each transducer successively pulsing while the others record the transmitted signal. In the active mode, a velocity survey is typically run every minute and the flight times of P-waves can be extracted and converted into velocity knowing the distance between source-receiver pairs. In the passive mode, we can analyze the acoustic emission (AE) activity during the experiment. We can also locate the micro-seismic events using a model of the velocity field in the rock sample inferred from the velocity surveys (active mode), but the results of this analysis will not be reported here.

3.2. *Experimental protocols*

In contrast with previous studies based mainly on triaxial testing to assess mechanical water-weakening effects in reservoir rocks, we promote an experimental protocol based on fluid injection, adapted from the work of Stanchits et al. [2011]. Three different fluids were used: air, water and oil. In the last case, we used Fluorinert oil, a fully-fluorinated liquid (no oxygen) which has at 25°C a density $\rho_o=1940 \text{ kg/m}^3$, a dynamic viscosity $\mu_o=0.024 \text{ Pa.s}$ and a surface tension $\gamma_o=0.018 \text{ N/m}$ (for comparison, water properties are $\rho_w=1000 \text{ kg/m}^3$, $\mu_w=0.00088 \text{ Pa.s}$ and $\gamma_w=0.072 \text{ N/m}$). The mechanical tests were run under a controlled temperature of 25°C.

Three types of experiments were carried out (**Figure 1**). All three were performed on pre-consolidated samples, i.e. hydrostatically loaded up to 25 MPa (well below the critical stress P^*) and unloaded down to 5 MPa. This pre-consolidation (step I in **Figure 1**) is applied to minimize the effect of variations in initial crack content and promotes a better reproducibility of the mechanical behavior from sample to sample. The three experimental protocols consist of:

a) Triaxial tests: We first performed a standard characterization of P-wave velocity and compressive strength sensitivities to the different fluids through standard triaxial tests (**Figure 1a**). For the dry test, the sample is kept at 5 MPa confining pressure and axial stress is increased up to failure at constant strain rate of 10^{-5} s^{-1} (step IV). For the tests with water and oil as pore fluid, we first evacuated the dry pre-consolidated sample for a couple of hours to remove the air from the pore space, then we injected the fluid at the bottom end of the sample with a controlled fluid pressure of 0.5 MPa until at least one pore volume of fluid bled through the top pore fluid line (step II). We achieve full saturation by increasing both the pore pressure to 2 MPa and the confining pressure to 7 MPa (step III) to dissolve any residual air trapped in the pores and ensure full saturation of the samples while keeping the same effective confining pressure as in the dry test. Finally, the axial stress was increased at a constant strain rate ($0.5 \cdot 10^{-5} \text{ s}^{-1}$) up to failure (step IV) while the confining pressure and pore pressure were kept constant. In the following, we will refer to these tests as TRX-a, TRX-o and TRX-w when the saturating fluid was air, oil or water, respectively.

b) Fluid injection tests into dry samples: These tests are designed to highlight the effect of fluid injection in a dry rock under constant triaxial stress (creep condition). At a confining pressure of 5 MPa, a dry sample is axially loaded to a differential stress level corresponding to 80% of the dry compressive strength (**Figure 1b**). At this constant stress, the sample is evacuated for 15 minutes at its top end and then either water or oil is injected at the bottom end with a controlled injection pressure of 0.5 MPa. In the following, we will refer to these experiments as INJ-wa and INJ-oa for water and oil injection into a dry sample respectively.

c) Fluid substitution tests: We inject water into an oil-saturated sample under constant triaxial stress; a test aimed at mimicking Enhanced Oil Recovery operations by water flooding an oil-saturated reservoir (**Figure 1c**). The oil saturation of the sample was achieved

according to step II of the triaxial test at a confining pressure of 5 MPa. We aimed initially at conducting the fluid substitution under conditions similar to step III in the other injection tests, i.e. at stress level corresponding to 80% of the dry strength. However, doing so led to the premature failure of several samples before the targeted critical load of 80% was reached. Thus we targeted a lower value of differential stress of 13 MPa, corresponding to 70% of the oil-saturated strength derived from TRX-o test. In addition, water injection into the oil-saturated sample was carried out at a constant flow rate from the bottom end, while maintaining a back pressure of 0.35 MPa at the top end of the sample. This modification of the protocol was implemented to ensure that the sample was fully oil-saturated prior to injecting water, which was not an issue for INJ-wa and INJ-oa. We selected an injection rate ($30 \text{ cm}^3/\text{h}$) at the bottom end of the sample so that the fluid pressure there never exceeded 1 MPa. Although the bottom end fluid pressure was not controlled in this test, the selected injection rate there and the back-pressure applied at the top end must have generated only a relatively small pore pressure gradient across the sample (0.65 MPa across 80 mm). In the following, we will refer to this experiment as INJ-wo.

4. Results of the triaxial tests

During the saturation stage prior the triaxial tests, a striking difference was found between water injection and oil injection in the dry samples. The passage of the water near the planes where the ultrasonic sensors are located (**Figure 2a**) induces a decrease in P-wave velocity for water injection (**Figure 2b**), whereas for oil injection we observe an increase (**Figure 2c**). During the pre-consolidation stage, the reproducibility is not ideal when looking at the strain at maximum pressure and after unloading down to 5 MPa (**Figure 3a**) which is probably due to (i) the initial stiffness of the samples at room pressure being significantly different, (ii) the

different amount of time the samples were allowed to rest (creep) at the highest pressure (25 MPa) and/or (iii) the heterogeneous nature of the studied rock. However the stiffness of the samples at high pressure is relatively similar as suggested by the slope of the pressure-strain curve during unloading. As the pre-consolidation stage was aimed at minimizing the effect of sample heterogeneity, we consider that for each sample the final strain after unloading down to confining pressure of 5 MPa corresponds to a reference state with respect to which further triaxial deformation and weakening effects are evaluated. Therefore, the initial axial strain in the triaxial loading stage was set to zero.

During the triaxial loading, the mechanical behavior of the Sherwood sandstone is clearly controlled by the nature of the fluid saturating the pore space because both the peak stress and the static elastic moduli are different in the three triaxial tests conducted under similar effective pressure conditions (**Figure 3b**, **Table 2**). The lowest peak stress is found for the water-saturated sample TRX-w (14.1 MPa), much lower than for the dry sample TRX-a (20.2 MPa). Sample TRX-o has an intermediate peak stress value (18.5 MPa). Clearly water has a strong weakening effect not only on the mechanical strength of Sherwood sandstone but also on its elastic moduli, if we compare the Young's moduli for TRX-a (4.3 GPa), TRX-o (4.1 GPa) and TRX-w (3.5 GPa). No change in Poisson's ratio between dry and water-saturated samples (0.3) is observed (**Table 2**), but a significant reduction is recorded for the oil-saturated samples (~0.2). The results on the mechanical strength and elastic parameters of the three samples suggest that oil has also moderate weakening effects, not as pronounced as water. All the samples failed in the brittle regime as expected at such low confining pressure, with post-failure stress-drop, onset of dilatancy near the peak stress and shear localization.

5. Results for fluid injection tests

This section reports the details of the injection stage (step III in **Figure 1b** or V in **Figure 1c**) after the rock samples experienced a pre-consolidation cycle and were critically loaded to 70-80% of their compressive strength.

5.1. Water injection into a dry sample

Different stages in the strain response of sample INJ-wa can be observed (**Figure 4**):

* Stage (P): in the preliminary stage, the rock is dry and water has not yet reached the bottom end of the sample. As a high differential stress is applied, creep is taking place.

* Stage (I): rapid creep starts as soon as water reaches the bottom end of the sample, accompanied by a sharp increase in AE activity. As usually observed in creep experiments, stage I corresponds to primary creep with a concave downward curvature of the strain vs. time plot. From this stage on, the volume of injected water (plotted as a fraction of pore volume in **Figure 4**) increases almost linearly.

* Stage (II): the strain response of the sample moves to secondary creep with a constant rate for almost 25 minutes, accompanied by a non-negligible increase in AE activity. The volumetric strain first increases (compaction), then reaches a plateau. Note that there is some uncertainty in defining the limits of stage (II).

* Stage (III): a clear acceleration of the axial strain typical of tertiary creep occurs, but without any significant increase in AE activity.

* Stage (F): a simultaneous sharp acceleration of the strains and the AE activity is observed, probably indicating the failure of the rock. We define this event as a mechanical instability leading to very large strains, both axial (shortening) and volumetric (compaction).

250 **Figure 5** presents the evolution of stress-strains and acoustic emission activity for the total
 251 duration of experiment INJ-wa with the sample response after the development of mechanical
 252 instability and a 3D reconstruction obtained from X-ray CT images of the sample after the
 253 test. The strong acceleration of the strain for sample INJ-wa (**Figure 5a**) was accompanied by
 254 a drop in the differential stress with a magnitude of several MPa because the actuator was
 255 unable to maintain the target 16 MPa differential stress after the occurrence of the mechanical
 256 instability. This differential stress drop is accompanied by an increase of the AE rate, which
 257 tends to reach a plateau when the sample shortening is about 8% (**Figure 5b**). The volumetric
 258 strain data suggests that the sample initially compacted before dilating at the very end of the
 259 experiment. However the volumetric strain should be considered with caution: indeed the
 260 axial strain is averaged over the total sample length while the radial strain is a local
 261 measurement in the central part of the sample. The upper part of the sample shows no sign of
 262 damage (**Figure 5c**), and the bedding is still visible and undisturbed, whereas the lower part
 263 has experienced intense damage through the development of conjugated shear bands. Cross-
 264 sections through planes 1 to 4 confirm this observation (**Figure 5c**). The arrival of water at the
 265 altitude of a given ultrasonic ray path results in a decrease of the corresponding P-wave
 266 velocity (**Figure 6**). Note that the oblique ray paths between Planes 1 and 2 are affected soon
 267 after the beginning of the injection. At the onset of the mechanical instability, a sharp drop in
 268 P-wave velocity is observed in Plane 2 and along the oblique ray path between Planes 2 and 3,
 269 suggesting that significant damage is located between these two planes in agreement with the
 270 post-mortem CT images (**Figure 5c**). Interestingly, the velocities above the plane 3 are not
 271 affected by the water migration while the mechanical instability develops; the velocity
 272 decrease associated with the arrival of the water at the level of this plane is identified after 90
 273 minutes of injection. Our results show that mechanical instability occurred when the volume

of injected water was equivalent to only 15% of the pore volume (**Figure 3**) when the upper part of the sample is still free of water.

5.2. Oil injection in a dry sample

Compared to test INJ-wa, the time scale of the test INJ-oa is much longer and covers several hours (**Figure 7**), because of the higher viscosity of Fluorinert compared to water, which requires a lower injection rate to maintain a similar fluid pressure of 0.5 MPa. No acoustic emissions have been recorded during oil injection (Macault, 2013). We can also identify different stages during the oil injection experiment:

- * Stage (P): the rock is dry and oil has not yet reached the sample, small creep takes place.

- * Stage (I): primary creep with a noticeably larger strain rate starts when the oil reaches the bottom end of the sample.

- * Stage (II): there is no clear transition between stage (I) and (II) and a rather constant creep rate is observed for about 4 hours. The volumetric strain is monotonically increasing and the rock is compacting.

- * Stage (III): a slow increase in strain rate typical of tertiary creep is observed but with no significant AE activity. As the experiment was stopped after 8 hours when oil started to flow out of the top end of the sample, it is not possible to extrapolate if this acceleration of the strain rate would have led to mechanical instability and failure.

The P-wave velocity evolution in test INJ-oa is similar in its kinetics to the one observed in INJ-wa, except that velocity rather increases when the oil reaches a plane where ultrasonic sensors are located, in agreement with the saturation stage in TRX-o (**Figure 2**). When comparing both injection experiments, it is clear that the nature of the injected fluid has a strong influence on the mechanical behavior of the rock and on its elastic response.

5.3. Fluid substitution test

The third injection experiment was designed to mimic a scenario commonly used during secondary oil recovery by water flooding in hydrocarbon reservoirs (Bertauld, 2014). After the pre-consolidation stage we saturated the sample with Fluorinert and then injected water (see protocol in **Figure 1c**).

* Stage (P): the rock is oil-saturated and water has not yet reached the sample (**Figure 8**). Creep takes place and, in contrast with tests INJ-wa and INJ-oa, stage (P) extends after the water starts invading the oil-saturated sample at time $t=0$.

* Stage (I): the onset of faster creep is delayed and becomes noticeable 6 minutes after water first enters the sample. In contrast with classical primary creep curves, creep in INJ-wo exhibits a concave upward curvature.

* Stage (II): again there is no clear transition between stages (I) and (II), and in both stages the strain vs. time plot exhibits a concave upward curvature instead of the classical linear evolution characterizing secondary creep. In stage (I) and beginning of stage (II) the volumetric strain increases then starts to decrease during stage (II) suggesting a transition from compaction to dilation. Note however that because the radial strain measurement is local, this transition might as well be linked to the arrival of the water at the sample mid-height where the radial strain is monitored: dilation may have started earlier in the lower part of the sample.

* Stage (III): the axial strain rate increases faster while the volumetric strain is decreasing, as expected during tertiary creep. Few acoustic emissions are recorded near the end of stage (III).

* Stage (F): a very sharp increase in acoustic AE activity and strain rates occurs during this stage, which is probably related to the development of a mechanical instability. The final axial strain reached before unloading was 1.4%.

As for test INJ-wa, water seems to have a weakening effect on the Sherwood sandstone in this experiment, which eventually led to a mechanical instability when the volume of injected water was equivalent to 56% of the pore volume, compared to 15% for INJ-wa. However the time of occurrence (35-31 minutes) and the amount of axial strain (0.5-0.57%) at the onset of failure are comparable for both experiments. A sharp stress drop at the onset of the mechanical instability is also observed, accompanied by an increase in AE activity (**Figure 9a**). On a 3D reconstruction of X-ray CT images of the sample post-mortem (**Figure 9c**), several fracture-like features resembling shear bands can be observed in the lower half of the sample. As for test INJ-wa (**Figure 5c**), radial damage patterns are observed on a cross section. A set of inclined fractures distributed axi-symmetrically around the injection point in the lower part of the sample is observed. When the water reaches the ray path of a given pair of ultrasonic sensors, the P wave velocity decreases (**Figure 10**), and at the onset of the mechanical instability an additional velocity decrease occurs for the sensors located in the lower half of the sample. In addition, the mechanical instability occurs when water is located well above the plane 3. The total velocity drop is smaller than in INJ-wa, probably because the velocity contrast between water and oil is much lower than between water and air.

6. Discussion

Water weakening has been evidenced in Sherwood sandstone through classical triaxial tests, and most importantly through injection tests aimed at mimicking more realistically the stress state, stress path and fluid-substitution scenarios experienced by an actual reservoir at depth. For the former type of tests it was found that at the selected confining pressure the compressive strength of the water-saturated rock was reduced by 30% compared to the dry rock, whereas a relatively smaller strength reduction of 8% is observed for the oil-saturated rock. For the latter type of tests we showed that water injection in the Sherwood sandstone

initially saturated with either oil or air and stable under a constant stress equivalent to 70-80% of its compressive strength triggers a mechanical instability leading ultimately to failure in a relatively short period of time (less than an hour). Such instability was not observed during oil injection after 8 hours of injection. For both water and oil injection, creep occurs during fluid substitution, with a much faster creep rate (more than an order of magnitude) when water is injected compared to oil.

Rock physics monitoring through the recording of AE activity and P-wave velocity evolutions was used to assess the development of damage and fluid substitution during the experiments. The P wave velocity decreases when water reaches the sensors planes (**Figure 2, 6 & 10**), whereas it increases for oil migration (**Figure 2**). We relate this observation to the contrasting wetting characteristics of the fluids, i.e. water is expected to be wetting while oil is expected to be non-wetting. When water invades the pore space, capillary forces enhance the driving force in addition to the applied injection pressure, and this potentially leads to trapping of the non-wetting phase and heterogeneous distribution of fluids. As mentioned in Section 2, the velocity of Sherwood sandstone at low water saturation is smaller than that of the dry rock. The elastic weakening mechanism reported by Pimienta et al. [2014] linked to the adsorption of water molecules at grain surfaces is possibly another explanation for the P wave velocity decrease in water injection tests. On the other hand, for oil injection capillary driving force does not pull up the oil into the sample during injection, and we expect less air trapping. However the estimation of the actual water or oil saturation in the injection experiments is not straightforward. The evolution of velocity informs us on the approximate location of the fluid front, but not on the geometry of the invaded region. A piston-like fluid front propagation would induce a sharp decrease or increase of the velocity when water or oil is injected, respectively. Based on the progressive evolution of the velocity measured along a given plane, we can rather expect a more complex geometry. Furthermore the fluid is injected at the

bottom of the sample through a hole in the bottom platen, and a “plume”-like fluid migration in the pore space is expected and would give a better description of the injection process. Concerning the passive monitoring, less acoustic emissions were recorded in the water injection experiments when oil was used as the starting pore fluid (**Figure 9a**) compared to air (**Figure 5a**) and we can only speculate possible explanations: (i) an enhanced attenuation of wave amplitudes associated with the higher viscosity of Fluorinert; (ii) a shift in the dominant frequency of the radiated waves outside the sensitivity range of the ultrasonic transducers (~ 0.5 MHz).

The following sections will focus on specific aspects of the observations reported in the previous sections in an attempt to shed light on the mechanisms taking place during these experiments, namely, the stability of the experimental conditions and stress paths during the injection; the variations in creep rates and evidence of fluid-induced weakening; the final macro-structure of the damaged samples.

6.1. Stability of the experimental conditions and stress paths during the injection tests

The objective of the fluid injection protocol was to highlight specifically the effects of physico-chemical interactions between the pore fluid and the mineral matrix of the rock, while minimizing the influence of well-known mechanical effects associated with changes in effective stress. In this regard, the main feature of this protocol is to carry out a fluid injection/substitution with a fluid pressure as small as possible so that during the injection: (i) the average effective confining pressure in the sample is not significantly affected; and (ii) the contrast in effective confining pressure between the fluid-invaded and the dry parts of the sample at any given time is minimized so that the stress heterogeneity remains low. Doing so, effective stress variations are not expected to be the major factor triggering the observed

mechanical instability, and therefore the observed weakening can reliably be attributed to the nature of the injected fluid.

Stanchits et al. (2011) in their study on the Flechtingen sandstone, which has a higher compressive strength than the Sherwood sandstone, applied higher injection pressures between 5 and 30 MPa. In these conditions, a concomitant effect of water weakening and stress-induced damage may be expected. In contrast, in both INJ-wa and INJ-oa, the fluid pressure at the bottom of the sample was maintained at a low value of 0.5 MPa during the injection (**Figure 11**), which induces a very small contrast in effective pressure between the dry and the fluid-invaded part of the sample (10% change). In INJ-wo the bottom pore pressure during injection raised up to about 1 MPa, while the back-pressure at the top end was maintained at 0.35 MPa. Note however that changing the injection protocol for the experiment INJ-wo resulted in a significant difference in fluid injection rate (30 cm³/h compared to INJ-wa and INJ-oa (3-4 cm³/h) while the impact of the injection rate on the damage induced by water weakening remains unknown. As in both water injection experiments failure occurred at a similar time, more water was present in the oil-saturated sample (**Figure 8**) than in the dry sample (**Figure 4**) when the mechanical instability and the resulting failure developed. In a sense water was more efficient in destabilizing the rock during the test INJ-wa than during the test INJ-wo.

To assess a potential role of effective pressure variation on the sample failure, we use the failure envelope obtained by Nguyen et al. [2014] for the water saturated Sherwood sandstone, which can be fitted by the cap model of Wong et al. [1997] (**Figure 12a**). Our results, in terms of followed stress paths and associated peak stresses, have been superimposed on the same plot. The failure stress for TRX-w is in good agreement with the data reported by Nguyen et al. [2014]: for sake of simplicity the failure envelope at low mean effective stress can be approximated by a straight line obtained by the least-squares best fit on

the three data points available for the water-saturated Sherwood sandstone (**Figure 12a**). We assume that a straight line with equal slope but different intercept (i.e. pore-fluid dependent cohesion) is also a good approximation for the failure envelope of the dry and oil-saturated Sherwood sandstone (**Figure 12b**). For the dry rock, this assumption seems to be fairly good: indeed the green solid circle in **Figure 12b**, corresponding to the failure stress reported by Nguyen [2012] for a triaxial test at 2 MPa confining pressure on a dry Sherwood sandstone sample, is in good agreement with the estimated straight line. Starting from the stress states at which the injection experiments have been performed (dashed lines), we report the stress paths associated with the fluctuation of pore pressure (**Figure 11**) imposed or induced during these tests; we obtain the orange and green horizontal paths in **Figure 12b**, respectively. We can see that both stress paths do not intercept the corresponding failure envelopes, which means that the observed mechanical instability was likely triggered by fluid weakening effects and not by the pore pressure change. This conclusion, drawn from the worst-case scenario where the failure envelopes are linear at low stresses, would be even stronger if one takes into account the curvature of the failure envelopes (**Figure 12a**) commonly observed in porous rocks [Wong et al., 1997].

6.2. Variation in creep rates and evidence of fluid-induced weakening

Water injection resulted in faster creep rates compared to oil injection (**Figure 13a**). Before the arrival of the injected fluid into the rock sample, creep rates are systematically small, comprised between 3.9 and $5 \cdot 10^{-8} \text{ s}^{-1}$ (**Table 3**). The largest rate was recorded during the injection of water in the oil-saturated sample (INJ-wo). During the oil injection test (INJ-oa), a moderate increase in creep rate is observed (from 3.9 to $4.4 \cdot 10^{-8} \text{ s}^{-1}$), whereas an increase by more than one order of magnitude occurred during the water injection test INJ-wa. For INJ-wo, the creep rate is accelerating continuously and a real secondary creep stage or a primary

creep with a concave downward curvature is absent. Therefore the values reported in **Table 3** for this test are approximations. The time at the onset of tertiary creep is comparable for both water injection tests, but much smaller than for the oil injection test (**Table 3**). For all three experiments the strain increment (measured strain minus strain at the beginning of creep) is almost the same, so that the onset of accelerated creep occurs more or less at the same level of damage accumulated in the early creep stages, as previously reported by Heap et al., 2009. During primary and secondary creep the strain vs. time plots for INJ-wa and INJ-oa are almost linear in logarithmic scale with a similar slope (**Figure 13b**). A power-law with a similar exponent must thus fit our results for these two experiments. The best fit creep law in stages I and II is given in **Table 3** for INJ-wa ($\epsilon(t) = 0.199 t^{0.84}$) and for INJ-oa ($\epsilon(t) = 0.0187 t^{0.92}$). The creep behavior for INJ-wo exhibits a transition from a slow creep at early times, similar to that observed in experiment INJ-oa, to a faster creep at larger times typically observed in experiment INJ-wa (**Figure 13b**). The sharp creep acceleration in INJ-wo seems to be similar in nature to that observed in INJ-wa, but occurs with a time delay. This transition phase occurs at a rate nearly double compared to that observed for both other tests. Tentatively we interpret this observation as a transition from a behavior dominated by oil-wet to a behavior dominated by water-wet solid surfaces during test INJ-wo, and this evolution does not follow the classical transition from primary to secondary creep. The results for water and oil injection in the dry samples display a similar behavior, which can be fitted by a single scaled creep law

$$\left(\frac{\epsilon}{\epsilon_t}\right) = \left(\frac{t}{t_t}\right)^{0.9}, \quad (1)$$

whereas the results for test INJ-wo clearly follow a different trend involving a time delay and significantly higher exponent

$$\left(\frac{\epsilon}{\epsilon_t}\right) = \left(\frac{t}{t_t}\right)^2 - \tau^2, \quad (2)$$

in which $\tau = 0.2$ corresponds approximately to the (normalized) delayed time when accelerated creep starts in this particular experiment (**Figure 13c**). In both equations, strain and time are normalized to their respective values ε_t and t_t at the onset of tertiary creep (**Table 3**). Equation (1) holds for both fluids injected in the dry sandstone: fluid weakening appears to be a scaling process for which water, compared to oil, enhances the magnitude (by a factor ε_t) and the rate (by a factor t_t) of the strain experienced by the rock, probably without intrinsically changing the micro-mechanisms of the deformation. Note however that t_t for INJ-oa is about 15 times larger than for INJ-wa; and that the ε_t values are similar for both experiments. This suggests that the large-time magnitude of strain associated with weakening due to water and Fluorinert are in fact similar in the dry Sherwood, but to reach this asymptotic strain magnitude it would take 15 times longer with Fluorinert than with water. In other words, if we had carried on with the test INJ-oa for a longer time (> 8 hours), the sample would probably have reached failure.

In contrast, when water is injected in the oil-saturated sandstone a very different creep law applies suggesting that the operating mechanisms leading to macroscopic creep might be different. Brantut et al. [2013] argue on the basis of the work by Main [2000] that secondary creep is in fact an intermediate transient stage between primary creep dominated by crack propagation with a negative feedback between crack length and K_I , the stress intensity factor in mode I, and tertiary creep where a positive feedback leads to accelerated creep and failure. Apparently this does not hold for the water into oil injection test where negative feedback seems to be missing. So far we have no definitive answer for such a contrasting behavior.

Water injection resulted in catastrophic failure in both experiments INJ-wa and INJ-wo but not in INJ-oa, confirming our conclusions from triaxial testing that fluid sensitivity and water weakening need to be taken into account in the mechanical behavior of Sherwood sandstone, effective pressure effects put aside. Baud et al [2000] analyzed the effect of water weakening

on the mechanical behavior of a set of sandstones with various degrees of quartz and clay contents: using fracture mechanics concepts they showed that the strength reduction in the presence of water can be linked to a decrease in surface energy γ which lowers both the fracture toughness K_{IC} (or equivalently the fracture energy G_C) and the friction coefficient μ , thus facilitating crack propagation and sliding. They argue that the strength decrease due to fluid weakening is controlled by the strength reduction parameter $\lambda = \gamma'/\gamma = (K'_{IC}/K_{IC})^2$, where primed symbols correspond to the parameters in presence of water. Water weakening will also induce a reduction in the critical pressure such that $P^{*'}/P^* = \lambda^{3/2}$. Applying this relationship to their tested sandstones, Baud et al [2000] found a strength reduction parameter λ in the range 0.79 to 0.97. For the studied Sherwood sandstone we only know the critical pressure $P^{*'} = 39.5$ MPa for water saturated conditions [Nguyen et al., 2014]. We can calculate λ from the strength reduction found in our set of triaxial experiments (**Figure 3** and **Table 2**). Comparison of strength reductions from dry to water-saturated and dry to oil-saturated conditions yields $\lambda_{wa} = 0.70$, and $\lambda_{oa} = 0.91$, respectively. These values allow for the prediction of the critical pressure for the dry rock ($P^* = 67.4$ MPa) and for the oil-saturated rock ($P^* = 45.5$ MPa). Due to the limitation of the used experimental rig, Nguyen et al. [2012] could not load dry Sherwood sample above 60 MPa and no evidence for onset of pore collapse was recorded at such confining pressure. The derived dry P^* is in agreement with this result. The reduced surface energy contrast when water substitutes oil in the pore space $\gamma'/\gamma_o = \lambda_{wa} / \lambda_{oa} = 0.77$ may explain the delayed creep acceleration in test INJ-wo but not the highest creep rate once it started. Our understanding of the deformation mechanisms during the injection tests is far from being sufficient, in particular because it was not possible to do post-mortem microstructure analyses (the samples could not be retrieved without complete loss of cohesion). One question that needs addressing in future studies is the specific role of clays in the weakening process.

522

523 *6.4. Strain localization patterns*

524 For both water injection experiments, we investigated the post-mortem damage patterns using
525 X-ray tomography techniques. For the test INJ-wa, a 3D reconstruction of the sample has
526 already been presented in **Figure 5c**: whereas the upper part of the sample did not show any
527 visible sign of deformation, the lower part has experienced important damage. For this
528 experiment, the overall axial strain at the end of the test was close to 10%. On a horizontal
529 section through the damaged zone, we observe numerous dark spots (low density, probably
530 large pores/discontinuities) as well as a pattern of bright radial linear structures (high density
531 zones) (**Figure 14a**). To our knowledge such radial features have not been observed in triaxial
532 loading experiments in consolidated rocks, but similar features were observed in triaxial tests
533 on unconsolidated granular materials. For example a CT scan image of sand packs loaded
534 under triaxial conditions shows similar patterns [Batiste et al., 2004] (**Figure 14b**). Similar
535 features have also been found experimentally by Desrues et al. [1996] and were reproduced
536 by Fazekas et al. [2006] using DEM numerical simulation on unconsolidated granular media.
537 This striking similarity provides new insight onto the damage mechanisms that occurred in
538 test INJ-wa. Due to the water invasion from the bottom, we think that a complete or partial
539 loss of cohesion between grains occurred in the lower part of the sample, while the upper part
540 remained mechanically stable. Looking at the curved interface between the damaged and the
541 intact zones in **Figure 5c**, it seems that the cohesive upper part of the sample acted as a hard
542 indenter on the cohesion-less lower part.

543 On the 3D reconstruction for test INJ-wo (**Figure 9c**), several shear bands, oblique and radial,
544 as well as axisymmetric circular features were observed. For this experiment, we recall that
545 the axial strain at the end of the test was lower than for INJ-wa, close to 1%. Again the
546 damage was concentrated in the lower part of the sample, while the upper part was virtually

undamaged. Based on the threshold of the CT scan images, we propose a 3D reconstruction of the damaged zone shown in **Figure 14c**: we can see that the damaged zone has a conical shape. The cone base corresponds to the bottom end of the sample and oblique shear fractures radiate from the center. Again there is a striking similarity with what has been observed by Desrues et al. [1996] in triaxial experiments on sand packs: a sketch of the deformation patterns found by these authors is shown in **Figure 14d**, with a central cone and V shaped fractures radiating from the cone surface. As stated by Desrues et al. [1996], such axisymmetric features are likely to develop in unconsolidated materials due to higher degrees of freedom in un-cemented grain packs compared to cemented sandstones. Like for the other water injection test INJ-wa, we suspect that the sample has experienced a loss of cohesion. Water seems to confer the properties of unconsolidated sand upon the invaded part of the sample. One may argue that these deformation patterns could be influenced by local stress variations due to friction between the sample and the piston: such effects can hardly be avoided in mechanical testing. However, damage was observed only in the region where water was injected and not near the top end of the samples, where friction effects also exist. This confirms that damage is primarily linked to fluid weakening.

Our data set is far from being exhaustive: only one rock type has been tested so far, under a single stress configuration and limited structural study could be achieved on the deformed samples. More work will be necessary to highlight the effect of fluid chemistry (especially salinity which has an important effect on swelling properties of clay minerals), temperature and stress state in order to get closer to realistic in situ reservoirs conditions.

7. Conclusions

We studied fluid-weakening effects on the weakly-consolidated Sherwood sandstone by conducting standard triaxial tests and fluid injection tests on critically loaded samples. Water weakening resulted in a 30% decrease of the compressive strength when comparing the results of triaxial tests on dry and water-saturated samples, at low effective confining pressure (5 MPa). Oil has also a weakening effect but with moderate amplitude (8% decrease in strength). Water weakening leads also to accelerated creep when injecting water into dry and oil saturated samples loaded up 70 to 80% of the compressive strength. Eventually tertiary creep is followed by the onset of a mechanical instability linked to the development of intense damage and loss of cohesion in the region where water has invaded the rock. In the injection tests the injection pressure was kept to a low value in order to minimize the effect of effective stress variations, so that the mechanical response could primarily be linked to the physico-chemical effect of the invading fluid. One major conclusion of our work is that water weakening is able to trigger mechanical instabilities under static loading. Active acoustic monitoring allowed us to follow the migration of the fluid front. Another article devoted to the detailed analysis of the velocity field variation and the location of acoustic events during fluid substitution is currently in preparation. We believe that experimental studies like the one presented here can have a strong impact for 4D seismic monitoring strategies during enhanced oil recovery operations at the reservoir scale and for a better understanding of the mechanical response and the micro-seismicity associated with water weakening effects.

Acknowledgments

We thank Jérôme Wassermann for technical assistance in the benchtop experiments and for many fruitful discussions. Bruce Maney is also acknowledged for his technical expertise with the triaxial rig used in this study. We thank also Lionel Esteban, who provided us with the CT-scan images. Many thanks to both reviewers for their comments, which helped to improve significantly the paper.

References

Atkinson, B.K., and Meredith, P.G. (1987) Experimental fracture mechanics data for rocks and minerals, in *Fracture Mechanics of Rock*, edited by B.K. Atkinson, 477-525, Academic, San Diego, Calif.

Batiste, S.N., Alshibli, K.A., Sture, S. and Lankton, M. (2004) Shear band characterization of triaxial sand specimens using computed tomography, *Geotech. Test. J.*, 27, doi: 10.1520/GTJ12080.

Baud, P., Zhu, W. and Wong, T.f. (2000) Failure mode and weakening effect of water on sandstone, *J. Geophys. Res.*, 105, 16371-16389.

Bertauld, D. (2014) Experimental study of the water-weakening effects on reservoir rocks, Final internship report - engineering degree in Earth Sciences, Polytech Paris UPMC.

Brantut, N., Heap, M.J., Meredith, P.G., Baud, P. (2013) Time-dependent cracking and brittle creep in crustal rocks: A review, *J. Struct. Geol.*, 52, 17-43, doi:10.1016/j.jsg.2013.03.007.

Desrues, J., Chambon, R., Mokni, M. and Mazerolle, F. (1996) Void ratio evolution inside shear bands in triaxial sand specimens studied by computed tomography, *Géotechnique*, 46, 529-546.

- 625 Donnez, P. (2012) Essentials of Reservoir Engineering vol. II, Ed. Technip, ISBN 978-2-
626 7108-1010-0.
- 627
- 628 Doornhof, D., Kristiansen, T.G., Nagel, N.B., Pattillo, P.D. and Sayers, C. (2006) Compaction
629 and Subsidence, *Oilfield Review*, 18, 3, 50-68.
- 630
- 631 Fazekas, S., Török J., Kertész, J. and Wolf, D.E. (2006) Morphologies of three-dimensional
632 shear bands in granular media, *Phys. Rev. E*, 74, doi: 10.1103/PhysRevE.74.031303.
- 633
- 634 Heap, M.J., Baud, P., Meredith, P.G., Bell, A.F. and Main, I.G. (2009) Time-dependent brittle
635 creep in darley Dale sandstone, *J. Geophys. Res.*, 114, B7, doi: 10.1029/2008JB006212.
- 636
- 637 Louis, L., David, C. and Robion, P. (2003) Comparison of the anisotropic behaviour of
638 undeformed sandstones under dry and saturated conditions, *Tectonophysics*, 370, 193-212,
639 2003.
- 640
- 641 Macault, R. (2013) Assessment of the water weakening effects and acoustic monitoring of
642 fluid motion in a weakly consolidated reservoir sandstone, final master degree report, EOST -
643 Univ. Strasbourg.
- 644
- 645 Main, I.G. (2000) A damage mechanics model for power-law creep and earthquake aftershock
646 and foreshock sequences, *Geophys. J. Int.*, 142, 151–161.
- 647
- 648 Nguyen, V.H. (2012) Compaction des roches reservoirs peu ou non consolidées : impacts sur
649 les propriétés de transport, PhD Thesis, 316 pp., University Cergy-Pontoise.

650

651 Nguyen, V.H., Gland, N., Dautriat, J., David, C., Wassermann, J. and Guélard, J. (2014)
 652 Compaction, permeability evolution and stress path effects in unconsolidated sand and weakly
 653 consolidated sandstone, *Int. J. Rock Mech. Min. Sci.*, doi:10.1016/j.ijrmms.2013.07.001, 67,
 654 226-239.

655

656 Nguyen, V.H., Gland, N., Dautriat, J. David, C. Guélard, J. and Wassermann, J. (2012)
 657 Experimental study and modeling of the hydromechanical behavior of a weakly consolidated
 658 sandstone under proportional triaxial compression, *proc. 46th US Rock Mechanics*
 659 *Symposium*, Chicago, 24-27 June, ARMA paper 12-430.

660

661 Orowan, E., The fatigue of glass under stress, *Nature*, 154, 341-343, 1944.

662

663 Pimienta, L., Fortin, J. and Guéguen, Y. (2014). Investigation of elastic weakening in
 664 limestone and sandstone samples from moisture adsorption, *Geophysical Journal*
 665 *International*, 199(1), 335-347, doi: 10.1093/gji/ggu257.

666

667 Rehbinder, P.A., Schreiner, L.A. and Zhigach, K.F. (1948) *Hardness Reducers in Drilling*,
 668 translated from Russian, 163 p., Counc. for Sci. and Ind. Res., Melbourne, Australia.

669

670 Risnes, R., Madland, M.V., Hole, M. and Kwabiah, N.K. (2005) Water weakening of chalk:
 671 mechanical effects of water-glycol mixtures, *J. Petrol. Sci. Eng.*, 48, 21-36,
 672 doi:10.1016/j.petrol.2005.04.004.

673

Sarout, J., Ougier-Simonin, A., Guéguen, Y. and Schubnel, A. (2010) Active and Passive Seismic Monitoring of Shales Under Triaxial Stress Conditions in the Laboratory, EAGE Shale Workshop extended abstract, doi: 10.3997/2214-4609.20145401.

Sarout, J., Esteban, L., Delle Piane, C., Maney, B., Dewhurst, D.N. (2014) Elastic anisotropy of Opalinus Clay under variable saturation and triaxial stress, *Geophysical Journal International*, 198, 1662-1682, doi: 10.1093/gji/ggu231.

Schmitt, L., Forsans, T. and Santarelli, F.J. (1994) Shale testing and capillary phenomena, *Int. J. Rock Mech. & Geomech. Abstr.*, 131, 5, 441-427.

Stanchits S., Mayr S., Shapiro S., Dresen G. (2011) Fracturing of porous rock induced by fluid injection. *Tectonophysics*, 503, 129-145.

Wong, T.f., David, C. and Zhu, W. (1997) The transition from brittle faulting to cataclastic flow in porous sandstones: Mechanical deformation, *J. Geophys. Res.*, 102, 3009-3026.

Zhu, W. and Wong, T.F. (1997) Shear-enhanced compaction in sandstone under nominally dry and water-saturated conditions, *Int. J. Rock Mech. & Min. Sci.*, 34, 3-4, paper n°364.

Figure and Table captions

Table 1: Mineralogical content and petrophysical properties of the Sherwood sandstone. For the mineralogy, the range of volumetric fraction and mean value are given, for the petrophysical properties, the average properties and standard errors from measurements on several rock samples are given.

Table 2: Description and results of the triaxial (TRX) and injection (INJ) tests.

Table 3: Analysis of creep parameters for the three injection tests. The starred values are given with caution (no real secondary creep for test INJ-wo).

Figure 1: Experimental protocol for a) triaxial tests, b) fluid injection tests in dry samples, and c) fluid substitution test.

Figure 2: a) Map of the 16 ultrasonic transducers distributed on 4 planes, b) P-wave velocity evolution during the saturation stage, normalized to the value in dry conditions for test TRX-w (water injection and c) for test TRX-o (oil injection).

Figure 3: Results from the triaxial tests. a) Hydrostatic pre-consolidation stage on three dry samples. b) Triaxial loading on the same samples saturated with water, air and oil respectively.

719

720 **Figure 4:** Results for the water injection test INJ-wa in a critically loaded dry sample. Time
 721 zero corresponds to the moment when the injected fluid starts to flow into the rock
 722 sample from the bottom at constant pressure (0.5 MPa).

723

724 **Figure 5:** Evolution of a) differential stress Q , acoustic emission activity and b) axial (ϵ_a),
 725 radial (ϵ_r) and volumetric (ϵ_v) strains for the whole experiment INJ-wa. The grey
 726 bar corresponds to the time interval in Figure 4. c) 3D reconstruction of the sample
 727 after test from X-ray CT images and cross-section images of the four ultrasonic
 728 sensors planes.

729

730 **Figure 6:** P-wave velocity evolution (normalized to the velocity before injection) vs. time
 731 during water injection in test INJ-wa. The vertical dashed line corresponds to the
 732 onset of the mechanical instability.

733

734 **Figure 7:** Results for the oil injection test INJ-oa in a critically loaded dry sample.

735

736 **Figure 8:** Results for the fluid substitution test INJ-wo with injection of water into a critically
 737 loaded sample saturated with oil.

738

739 **Figure 9:** Evolution of a) differential stress Q , acoustic emission activity and b) axial (ϵ_a),
 740 radial (ϵ_r) and volumetric (ϵ_v) strains for the whole experiment INJ-wo. c) 3D
 741 reconstruction of the sample after test from CT-scan images and cross-section
 742 images of the four ultrasonic sensors planes.

743

Figure 10: P-wave velocity evolution (normalized to the velocity before injection) vs. time during the fluid substitution test INJ-wo.

Figure 11: Evolution of pore pressure, confining pressure, differential stress, mean effective stress and injection rate during the three injection tests.

Figure 12: a) Failure envelope for the water saturated Sherwood sandstone: the experimental data (open squares) from Nguyen et al. [2014] can be modeled using the cap model (solid and dashed brown lines) of Wong et al. [1997]. The red dashed line is the triaxial stress path followed in our study, the stars correspond to the peak stress for the TRX experiments shown in Figure 3 and the blue line is a linear approximation of the failure envelope. b) Closer view on the stress paths followed during pore pressure build-up in the injection tests. The failure envelopes for each saturating fluid are approximated by straight lines. An additional data point (green solid circle) from Nguyen [2012] has been added.

Figure 13: Comparison of creep plots for all three injection tests. a) Incremental strain vs. time in linear coordinates. The inserted figure is a close-up on the water injection tests. b) Same plot in logarithmic coordinates. c) Scaled creep plot with time and strain normalized by the respective values at the onset of tertiary creep.

Figure 14: Damage patterns induced by mechanical instabilities. a) Cross-cut in the damaged zone for test INJ-wa. b) CT-scan image of a sand pack sheared in a triaxial experiment (adapted from Batiste et al. [2004]). c) 3D reconstruction of the radial and conical fracture patterns in test INJ-wo. d) Sketch of the deformation patterns

769 observed in sand packs sheared in triaxial experiments (adapted from Desrues et al.
770 [1996]).

Mineralogical content		Petrophysical properties	
Quartz	26-44 % (30%)	porosity	$30.2 \pm 1.7 \%$
Felspar	13-26 % (18%)	bulk density	$1800 \pm 20 \text{ kg/m}^3$
Detrital clays (mainly illite)	3-29 % (12%)	grain density	$2590 \pm 30 \text{ kg/m}^3$
Mica	0-7 % (2%)	permeability // bedding (water flow method)	$350 \pm 70 \cdot 10^{-15} \text{ m}^2$
Heavy minerals	< 3 %	permeability perp. bedding (water flow method)	$200 \pm 30 \cdot 10^{-15} \text{ m}^2$
		Young's modulus (for dry rock)	$4.6 \pm 0.7 \text{ GPa}$

Table 1

Test name	Description	pore fluid in triaxial stage	Max. differential stress Q_{max} (MPa)	Young's modulus E (GPa)	Poisson's ratio ν
TRX-a	Full triaxial on a dry sample	Air	20.2 ("Dry" peak stress)	4.3	0.30
TRX-o	Full triaxial on an oil-saturated sample	Oil (Fluorinert)	18.5 ("Oil" peak stress)	4.1	0.23
TRX-w	Full triaxial on a water-saturated sample	Water	14.1 ("Water" peak stress)	3.5	0.31
INJ-wa	Water injection into a dry critically loaded sample	Air	16 (80% dry peak stress)	4.7	0.30
INJ-oa	Oil injection into a dry critically loaded sample	Air	16 (80% dry peak stress)	3.9	0.30
INJ-wo	Water injection into an oil-saturated critically loaded sample	Oil (Fluorinert)	13 (70% oil peak stress)	5.8	0.19

Table 2

777

Test name	<i>INJ-wa</i>	<i>INJ-wo</i>	<i>INJ-oa</i>
Load	16 MPa (80% "dry" strength)	13 MPa (70% "oil" strength)	16 MPa (80% dry strength)
Creep rate before injection (s^{-1})	$4.2 \cdot 10^{-8}$	$5.0 \cdot 10^{-8}$	$3.9 \cdot 10^{-8}$
Creep rate during injection - stage II (s^{-1})	$5.8 \cdot 10^{-7}$	$1.2 \cdot 10^{-6*}$	$4.4 \cdot 10^{-8}$
Creep law in stage I + II	$0.199 t^{0.84}$	-	$0.0187 t^{0.92}$
Time t_i at onset of tertiary creep (min)	28	22*	372
Strain increment ε_i at onset of tertiary creep (%)	0.11	0.094*	0.10
Onset of mechanical instability	yes	yes	no
Time at the onset of mechanical instability (min)	35	31	-
Strain increment at the onset of mechanical instability (%)	0.186	0.233	-
injected volume / pore volume at the onset of mechanical instability	15%	56%	-
Comments	standard creep (I, II, III), compaction	accelerated creep, compaction then dilation	standard creep (I, II, III), compaction, no AEs

778

779

Table 3

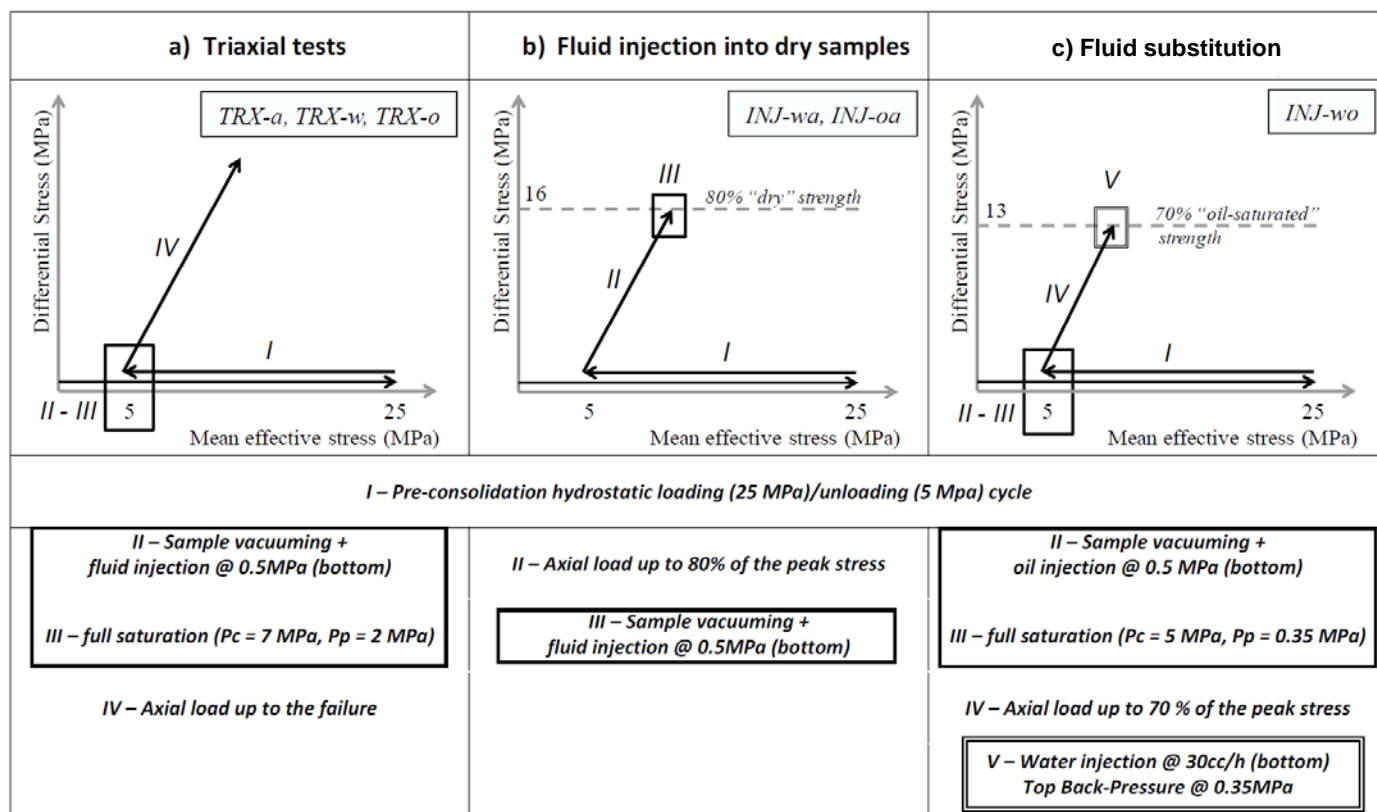


Figure 1

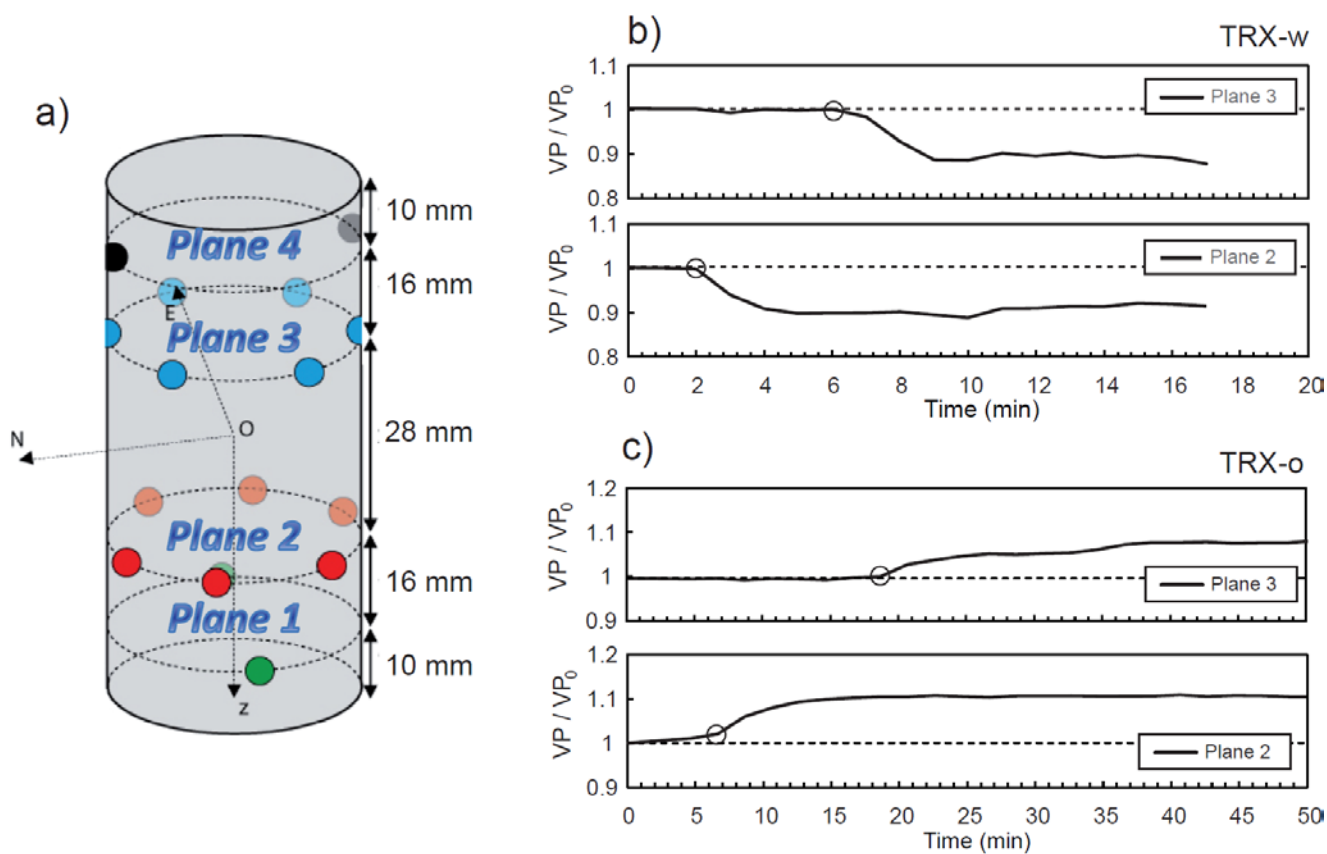


Figure 2

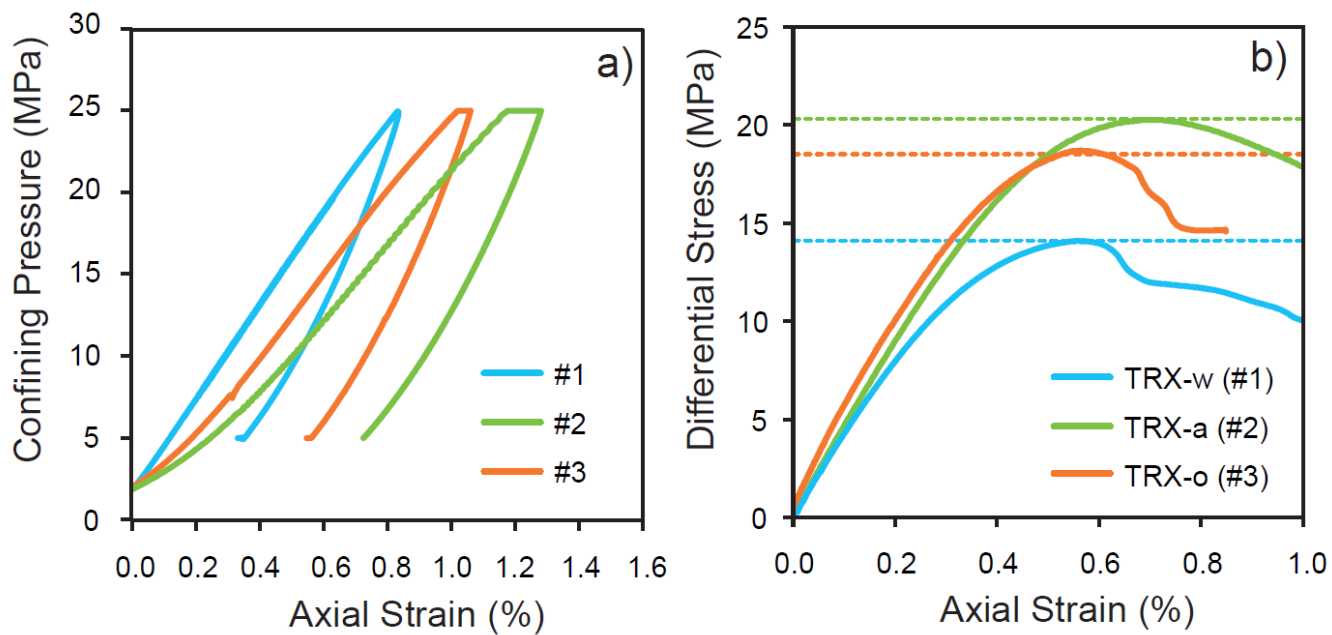


Figure 3

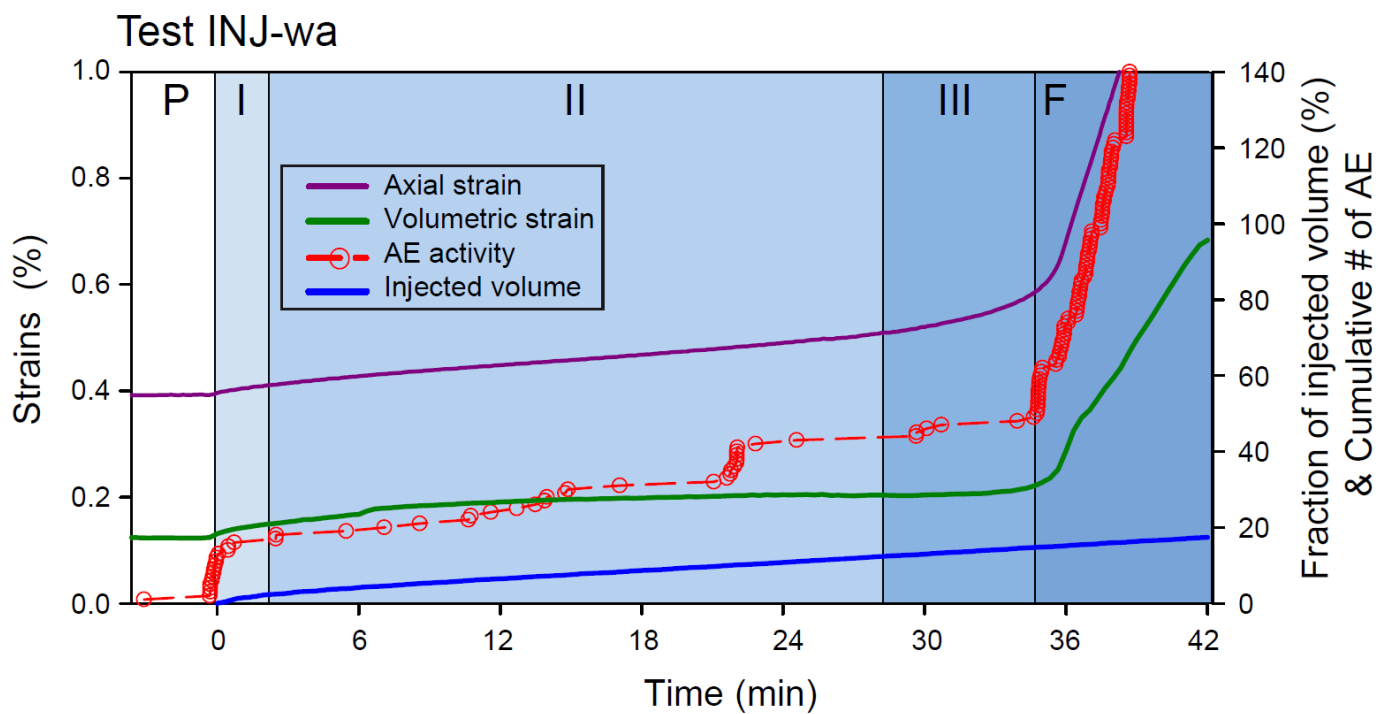


Figure 4

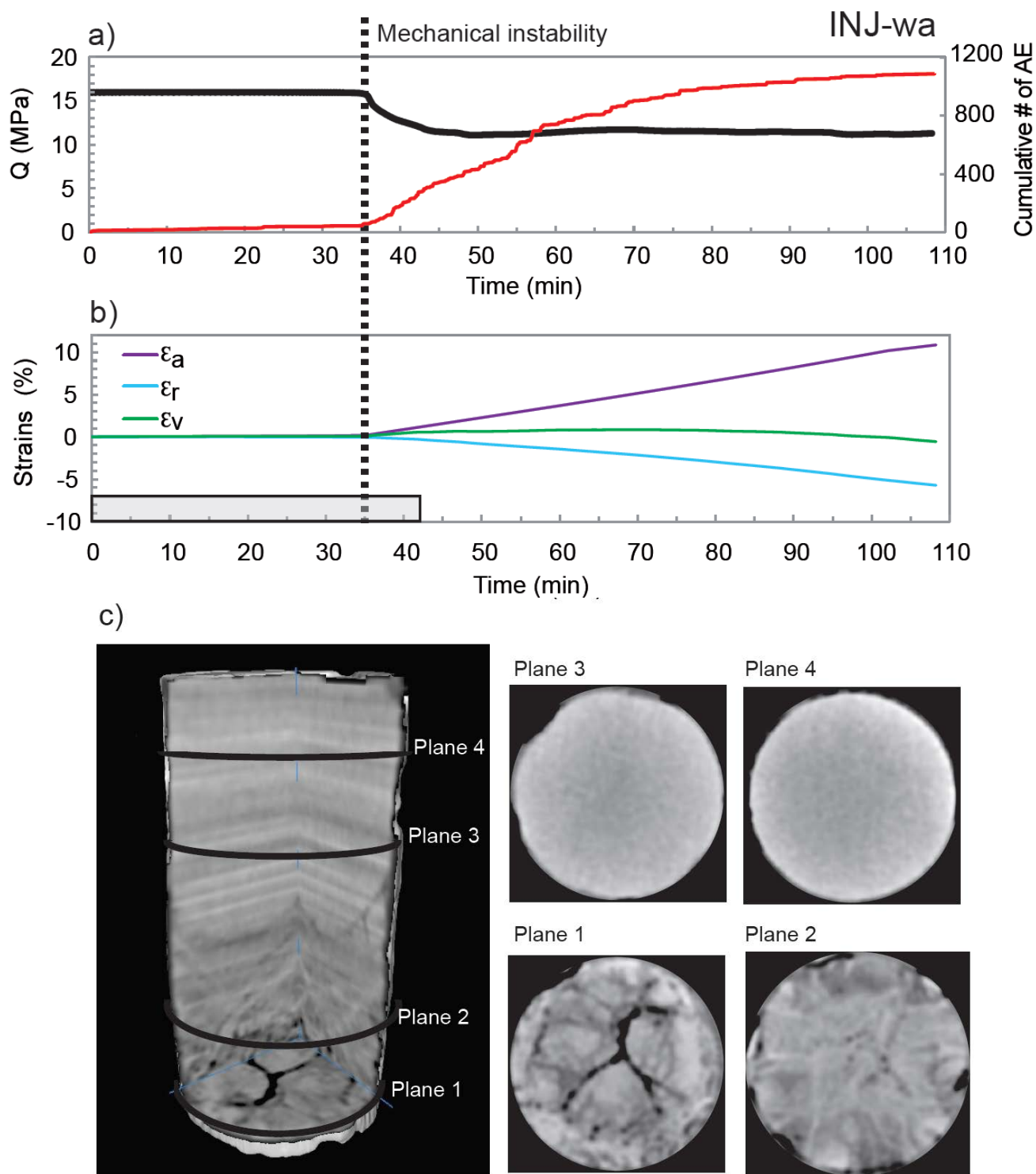


Figure 5

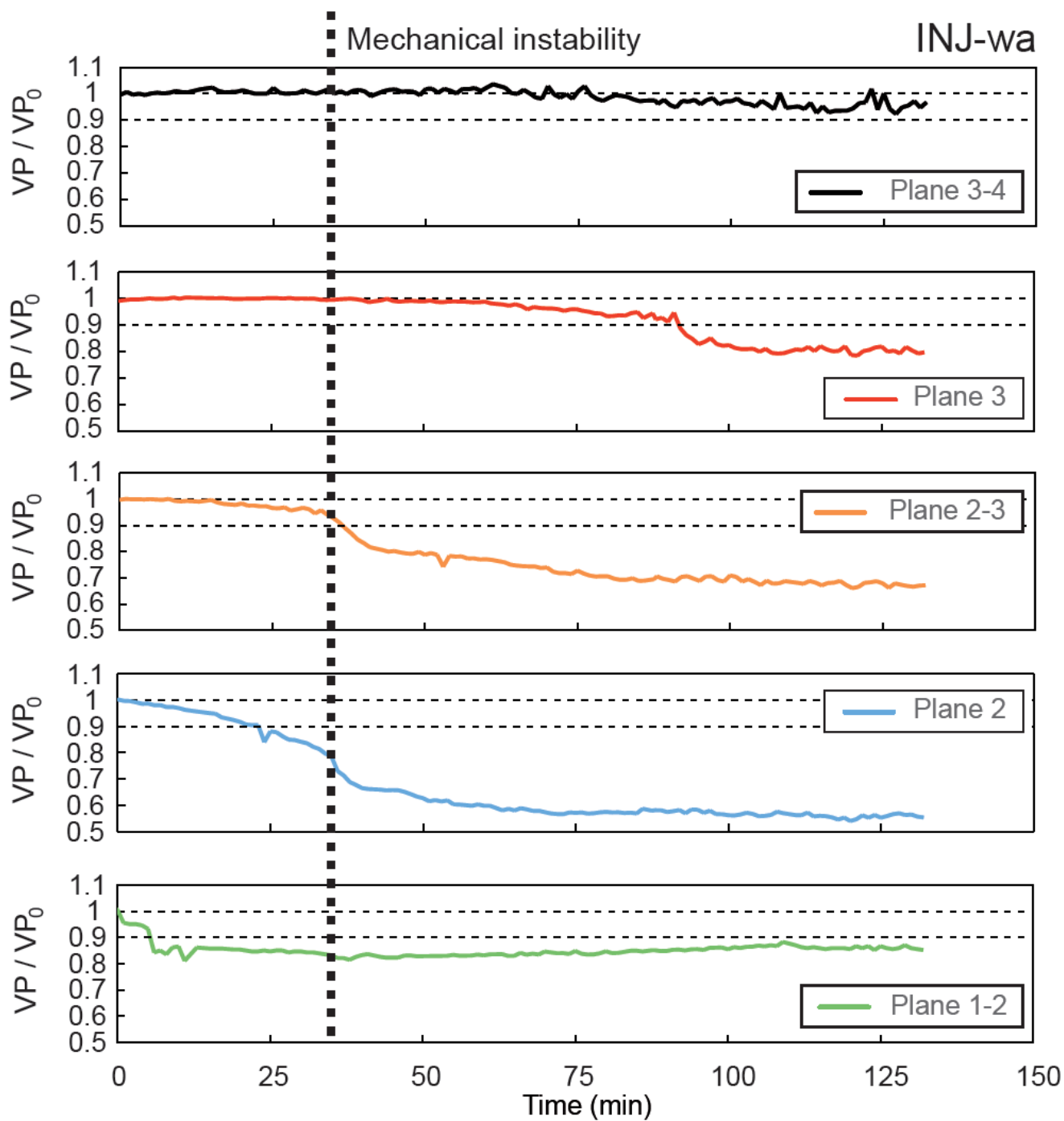


Figure 6

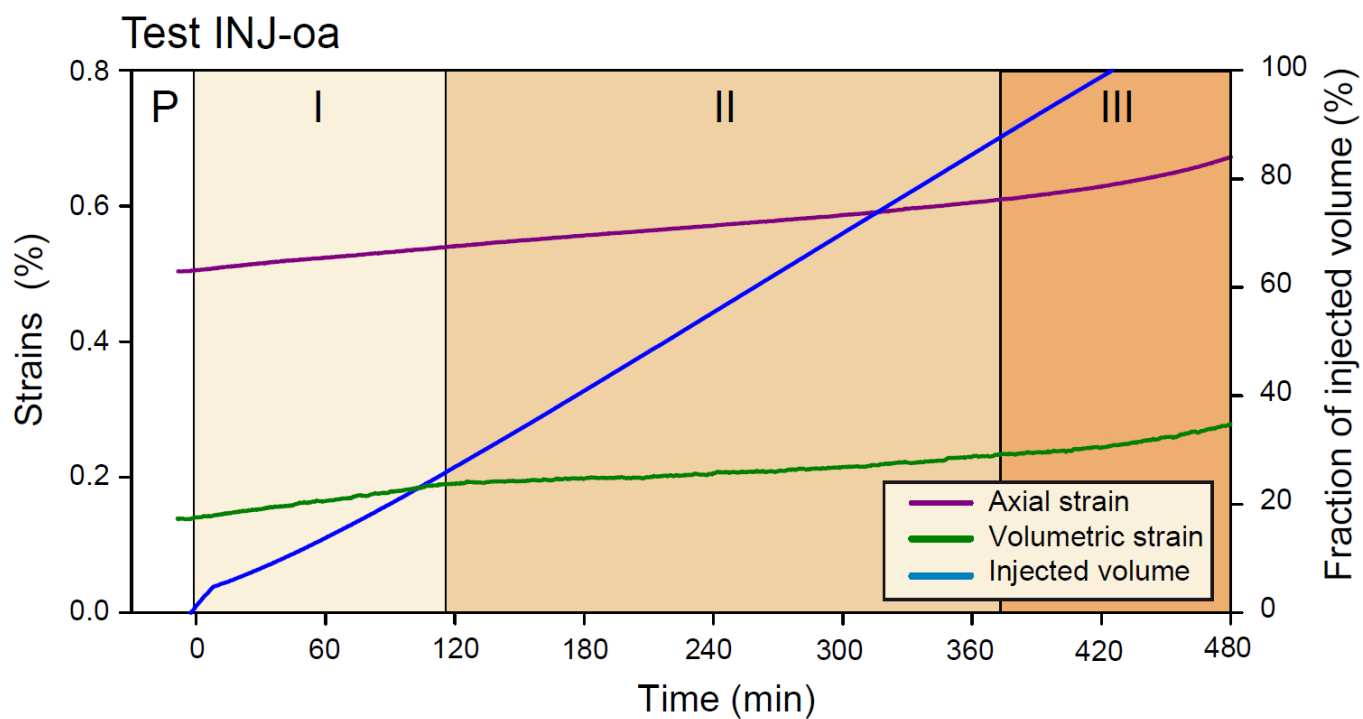


Figure 7

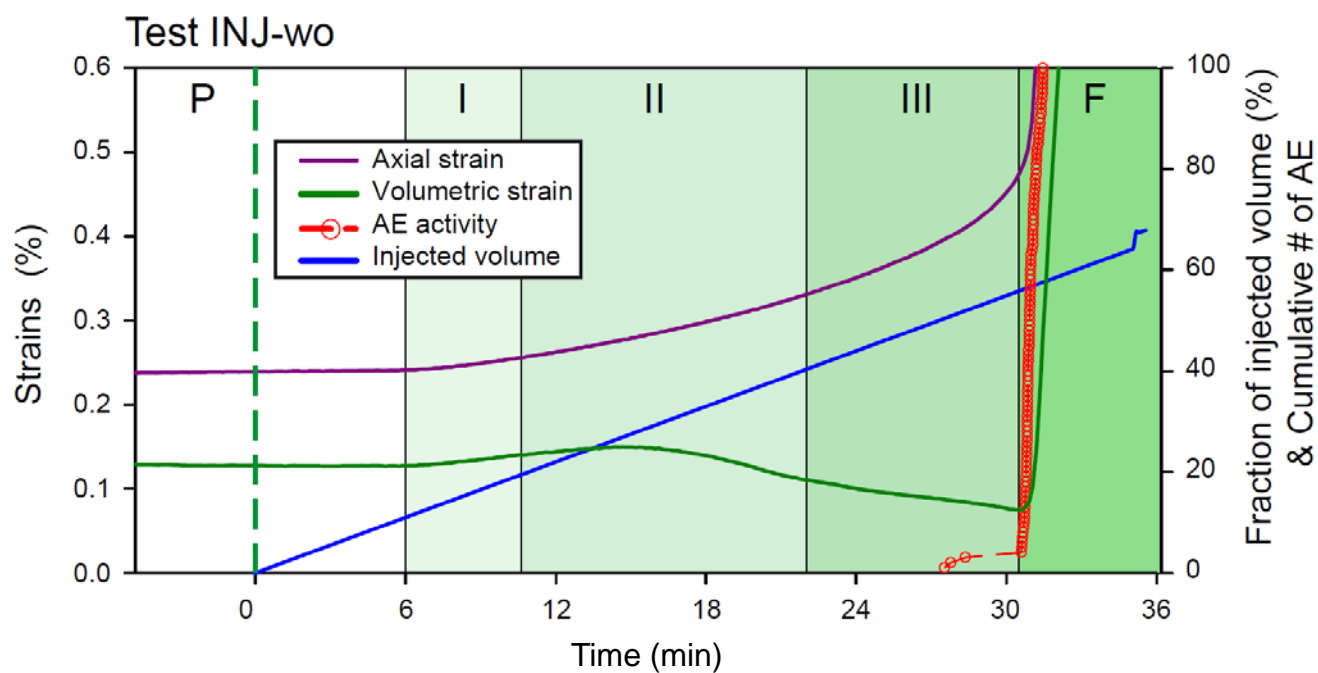


Figure 8

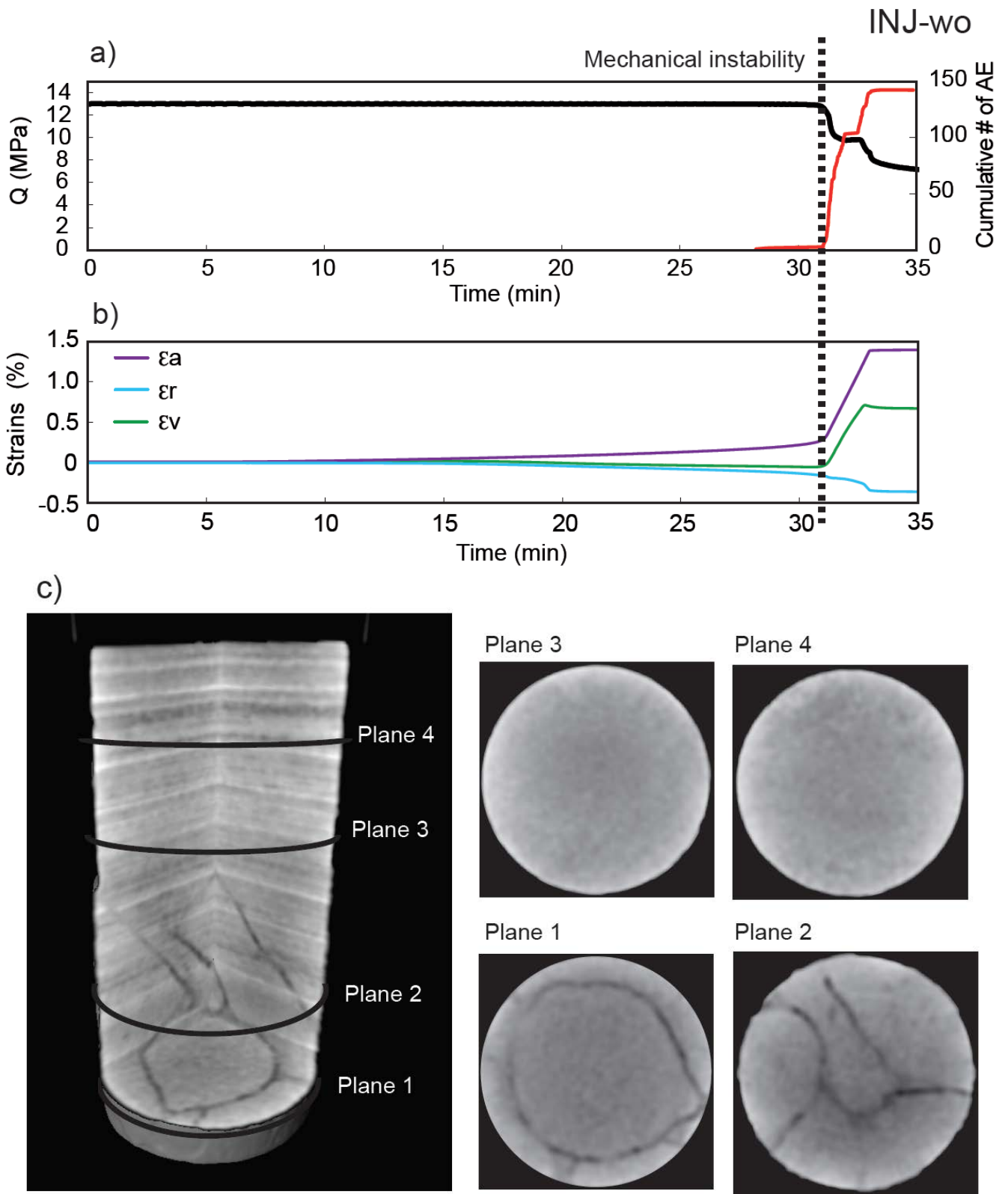


Figure 9

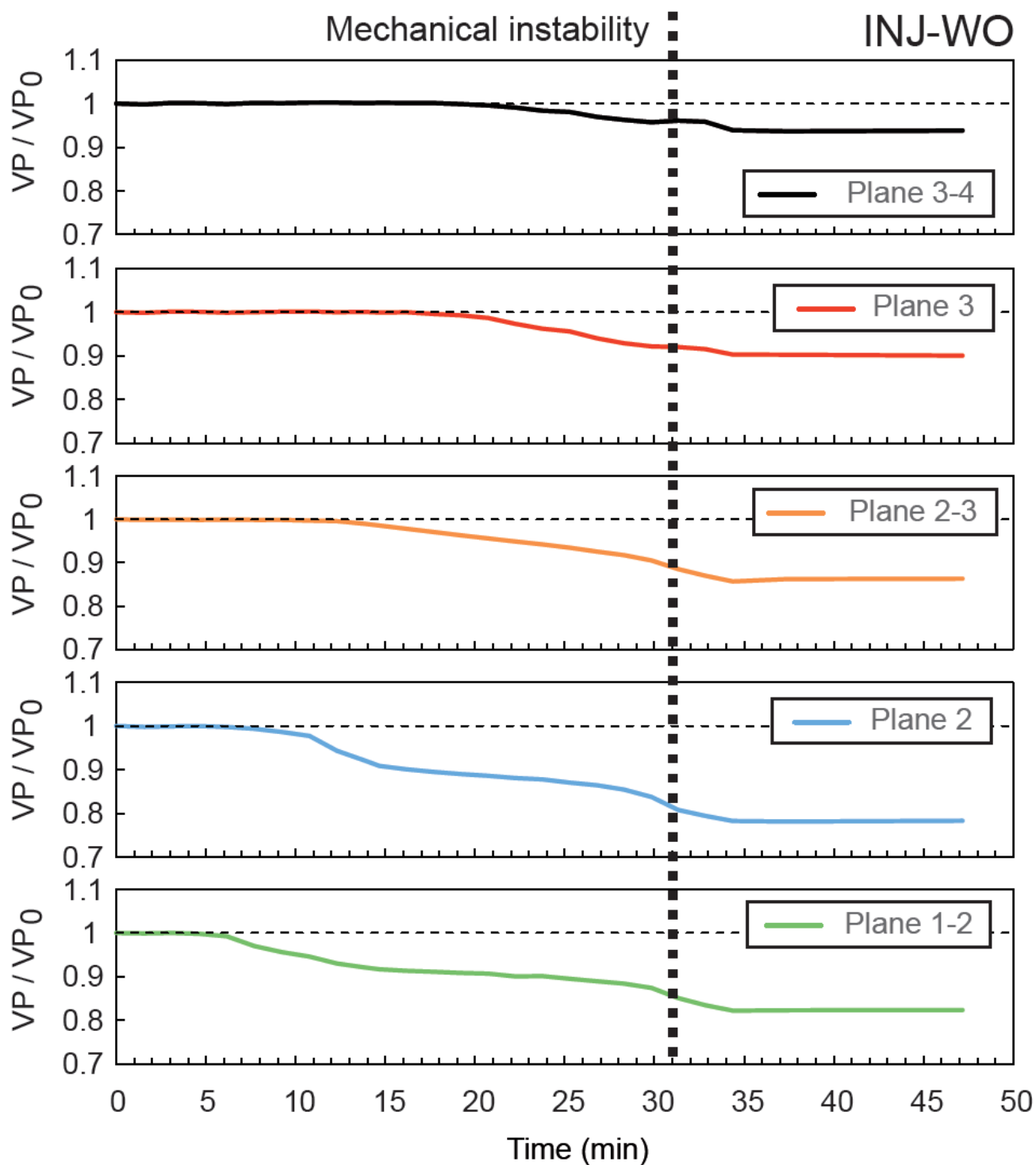


Figure 10

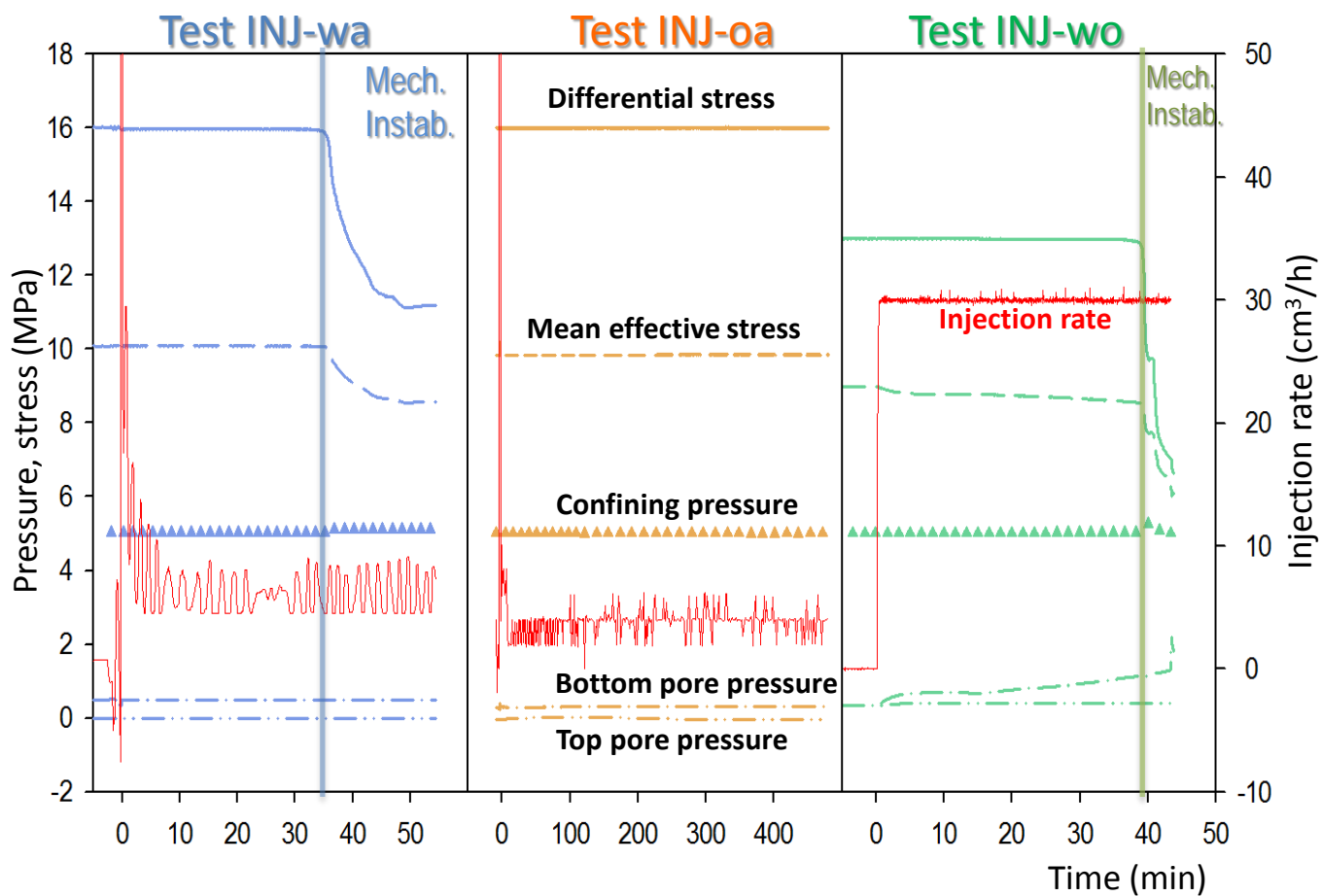


Figure 11

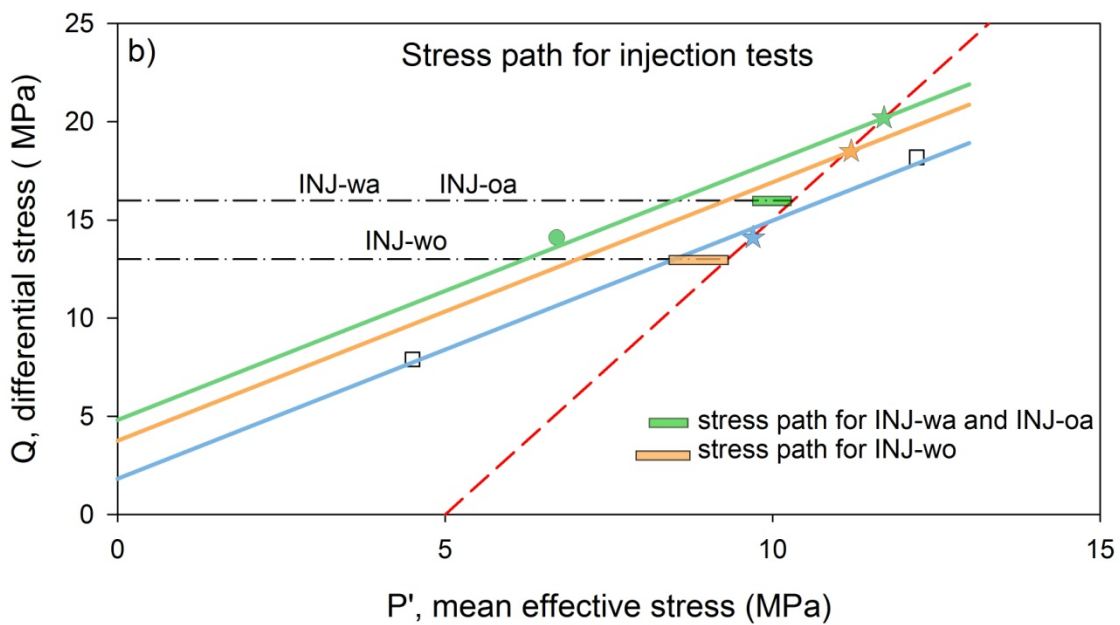
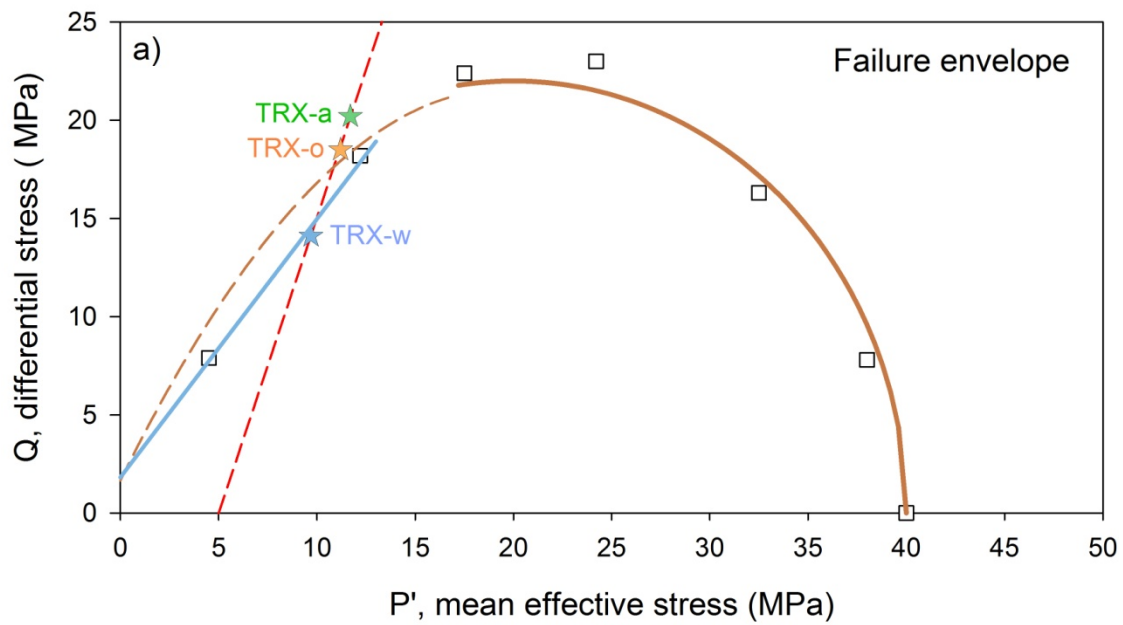


Figure 12

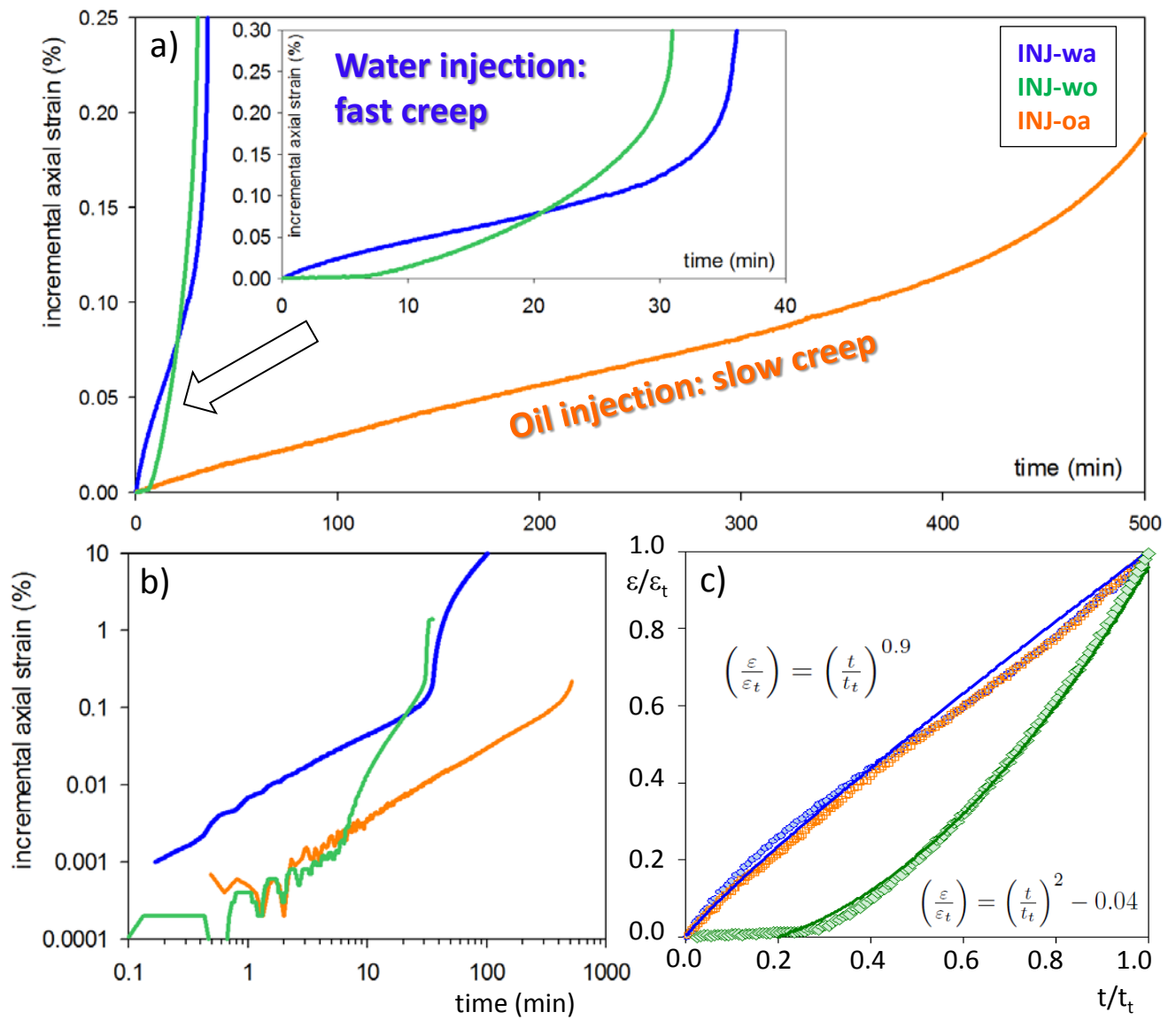
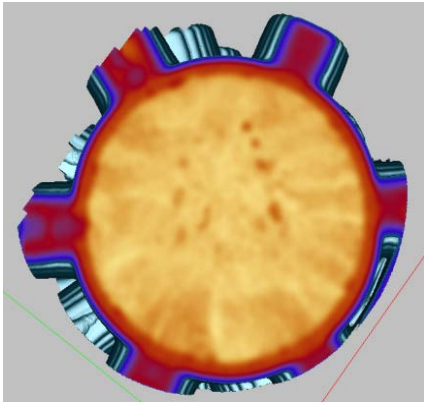


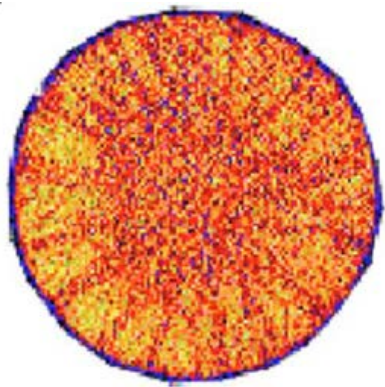
Figure 13

a)

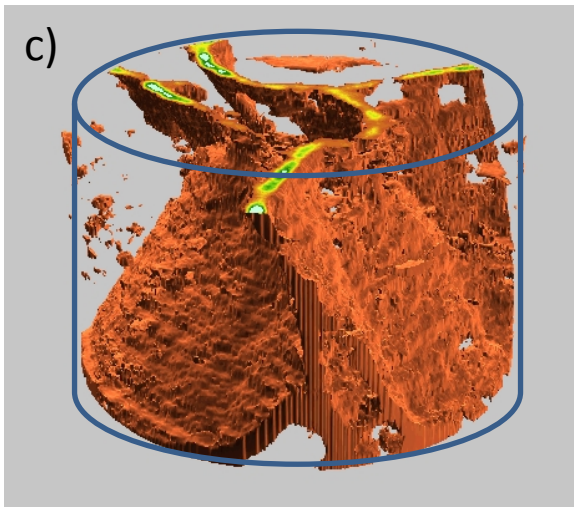


Test INJ-wa

b)



c)



Test INJ-wo

d)

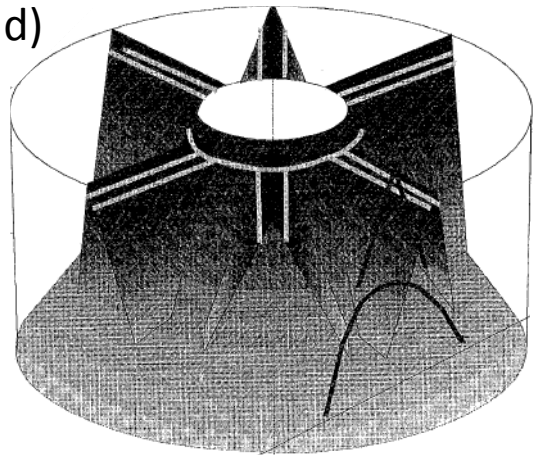


Figure 14